Journal of Materials Chemistry A

ROYAL SOCIETY OF CHEMISTRY

PAPER

View Article Online
View Journal | View Issue

Cite this: *J. Mater. Chem. A*, 2020, **8**, 19522

Basal plane activation in monolayer $MoTe_2$ for the hydrogen evolution reaction *via* phase boundaries†

Yiqing Chen, Pengfei Ou, Xiaohan Bie and Jun Song *

Received 22nd June 2020
Accepted 22nd August 2020

DOI: 10.1039/d0ta06165d

rsc.li/materials-a

Two-dimensional transition metal dichalcogenides (2D TMDCs) have attracted tremendous interest as a prominent material group providing inexpensive electrocatalysts for the hydrogen evolution reaction (HER). In the present study, using monolayer $MoTe_2$ as a representative, we demonstrated that phase boundaries can provide a viable pathway to activate the basal plane of 2D TMDCs for enhanced HER performance. Comprehensive first-principles calculations have been performed to examine the energetics and structural stabilities of possible 2H/1T′ phase boundary configurations. Three categories of sites, Te, Mo and hollow sites, have been identified at energetically stable phase boundaries, as potential catalytic centers for the HER, all indicating enhanced HER activity compared to that of the pristine basal lattice. In particular, the hollow sites, a new group of sites induced by phase boundaries, show great promise by exhibiting a Gibbs free energy (ΔG_H) near the thermoneutral value for hydrogen adsorption, comparable to that of Pt. The mechanisms underlying hydrogen adsorption at phase boundaries were then revealed, shown to be attributed to the unique local hydrogen adsorption geometries and electronic structures at phase boundaries. Our study clarifies the important mechanistic aspects underlying hydrogen activation at phase boundaries, providing valuable theoretical insights into designing a new class of high-performance HER electrocatalysts based on 2D TMDCs.

Introduction

Electrochemical water splitting is of particular importance to the production of hydrogen, crucial for the global goal towards clean energy economy and sustainability.[1] One core challenge in research efforts on water splitting is to identify efficient catalysts to facilitate evolution of H_2, *i.e.* hydrogen-evolution reaction (HER). Currently, platinum (Pt) and Pt-based materials are regarded as the *de facto* standard catalysts for the HER, but suffer from high cost and material scarcity, which hinder their large-scale utilization.[2,3] Therefore, there have been great efforts for studying alternative, non-Pt catalysts with low cost and high performance.[4] Among various potential non-Pt catalyst candidates, monolayer transition-metal dichalcogenides (TMDCs) are found to be effective towards the HER.[5–8] For instance, theoretical and experimental studies have suggested that monolayer MoS_2 can catalyze the HER at a moderate overpotential of 0.1–0.2 V with a Gibbs free energy of adsorption close to zero (<0.1 eV) at its edge sites.[9]

However, for monolayer TMDCs, the active sites for the HER are limited to the edge sites while the basal plane is inert, rendering the large surface area catalytically useless.[10,11] Such a limitation has motivated a great quest aiming to activate the basal plane of TMDCs.[12,13] One popular method which resulted from the quest is the introduction of (point) defects into TMDCs, which has been shown to lead to significant enhancement in HER activity.[10,13–16] Yet, with the introduction of defects come abundant dangling bonds at defect sites, which may poison the HER and cause structural instabilities.[17] A few other studies have suggested the approach of transforming TMDCs from the semiconducting 2H phase to the metallic 1T(or 1T′) phase. This 2H → 1T(1T′) phase transformation is shown to provide numerous active sites in the basal plane and at the same time improves the electrical conductivity of TMDCs.[18–20] However, the 1T(1T′) phase of most TMDCs is metastable and can easily revert back to the 2H phase.[21] More recently, Zhu *et al.* demonstrated in their experimental study that the basal plane of monolayer MoS_2 can be activated by introducing phase boundaries.[17] This facile route can provide a high density of active sites while retaining the structural stability by 2H–1T phase integration.[22] This provides promising new avenues towards basal plane activation of TMDCs without decreasing the structural stability.

Phase boundaries in TMDCs can be controllably induced *via* several methods, *e.g.*, thermal treatment,[23–25] particle irradiation,[26] and strain engineering.[27–29] Meanwhile, it is worth noting that, for group-VI TMDCs, the 1T′ phase is energetically more favourable than the 1T phase. Therefore it is reasonable to expect that, compared to 2H/1T phase boundaries, 2H/1T′

Department of Mining and Materials Engineering, McGill University, Montreal H3A 0C5, Canada. E-mail: jun.song2@mcgill.ca

† Electronic supplementary information (ESI) available. See DOI: 10.1039/d0ta06165d

phase boundaries would be thermodynamically more preferable, and are more likely to meet the requirement for structural stability and large-scale synthesis. Among the big family of monolayer TMDCs, $MoTe_2$ is an appealing candidate for achieving 2H/1T′ phase boundaries[30–32] because of the small energy difference between the 2H and 1T′ phases.[31] Therefore thermodynamically it is expected that the phase boundaries in $MoTe_2$ are relatively easy to form, and indeed they have already been successfully synthesized by chemical vapor deposition (CVD)[33] and heteroepitaxy.[30] In addition, several studies on Schottky metal–semiconductor junctions have reported improved catalytic activity by local charge redistribution. As a result, the respective semiconducting and metallic characteristics of 2H and 1T′ $MoTe_2$ together might synergistically lead to enhancement in the HER in the boundary region.[34–36] Previous studies have also shown that $MoTe_2$ phase boundaries exhibit excellent electrical properties,[33,37,38] an important factor that influences the overall catalytic activity towards the HER.[39] It was reported that the atomically coherent contact within 2H/1T′ $MoTe_2$ and the contact between 1T′ $MoTe_2$ and the current collector (*e.g.* Au electrodes) exhibited a low Schottky barrier height and thus low contact resistance.[30,40] The high conductivity of $MoTe_2$ and negligible contact resistance at the boundaries contribute to a fast electron transfer speed[39,41,42] and hold promise for the engineering of high-performance electrocatalysts in the future.

However, in contrast to numerous studies on isolated defects and edges in TMDCs with respect to the HER, research work on phase boundaries has been rather scarce, except for some recent studies examining specific phase boundaries in MoS_2 to show the existence of active sites on S atoms for hydrogen adsorption to potentially enhance HER activity.[17,43] Consequently, knowledge regarding the HER at phase boundaries in TMDCs remains largely absent, necessitating dedicated studies. Aiming at this, here in this paper, we perform systematic density functional theory (DFT) calculations to investigate HER activities at the phase boundaries in $MoTe_2$ as a representative TMDC system. Possible 2H/1T′ phase boundaries are constructed to examine their structural stabilities. Various candidate adsorption sites, namely Te, Mo and hollow sites, are explored in stable configurations. Our calculations show that all adsorption sites at $MoTe_2$ phase boundaries are activated, with the hollow sites as the most active sites for the HER and exhibiting outstanding HER activity comparable to Pt. Besides, we propose mechanisms to understand such activation at the phase boundaries. Hydrogen adsorptions at the Te sites are interpreted and predicted using the Fermi-abundance (D_F) model while the adsorption at Mo and hollow sites is qualitatively understood by analyzing the local charge distribution and density of states. The HER activity at the phase boundary was shown to be strongly dependent on the local hydrogen adsorption geometry and electronic structures.

Method and model

Monolayer $MoTe_2$ has three polymorphs, semiconducting 2H phase, and metallic 1T and 1T′ phases. Fig. 1(a) and (b) show the trigonal prismatic 2H phase consisting of 1×1 unit cells, and the distorted octahedral 1T′ phase with zigzag chains consisting of 2×1 supercells. It is worth noting that the 1T phase of $MoTe_2$ is metastable and would readily transform into the 1T′ phase, and therefore is not discussed in our study. Based on 2H and the 1T′ phases, a series of 2H/1T′ phase boundaries are constructed (for details see ESI S2†). In describing the phase boundaries, the naming convention used in the study of Zhao *et al.*[44] is used but modified accordingly to fit our 2H/1T′ case. A phase boundary is thus named in the form $D_M(-A-B)|S$, where D represents the direction of a $MoTe_2$ phase boundary, being zigzag (ZZ) or armchair (AC), with its subscript M denoting the type of atom (Te or Mo) shared by two phases at the boundary, and S indicates whether the phase boundary is rich in Te ($S = +$) or deficient in Te ($S = -$). A and B represent the types of edge configurations for 2H and 1T′ nanoribbons respectively at the phase boundary. There are four edge configurations, *i.e.*, α, β, C and T for a phase boundary along the ZZ direction (see Fig. 1(a) and (b)). On the other hand, since all the phase boundaries along the AC direction have the same edge configurations, the form is thus simplified to $AC_M|S$ only.

Fig. 1(c) shows the configurations of the stable phase boundary structures after geometry relaxation. Fig. 1(d) further illustrates a couple of sample relaxed structures of ZZ and AC phase boundaries in both top and side views. It is worth noting that for ZZ phase boundaries, the D_{3h} symmetry of 2H MoS_2 inevitably leads to different edge structures at both ends of a 2H MoS_2 nanosheet. Thus, periodicity along the ZZ direction would result in two different phase boundaries (for details see the ESI†), which however would make accurate evaluation of the phase boundary formation energy difficult. To address such a challenge, for ZZ phase boundaries, we construct a nanoribbon-like structure instead of a fully periodic sheet, as suggested in the study of Zhou *et al.*,[45] containing one phase boundary in the middle while one 2H edge and one 1T′ edge at each end. The dimension of the vacuum space along the non-periodic direction is set to be larger than 20 Å to ensure no image interaction. Meanwhile benchmark calculations have been performed to ensure that the separation between the nanoribbon edges is sufficiently large to avoid any artificial effect arising from edge–edge or edge–boundary interactions (for details see Section S1 in the ESI†). On the other hand, for AC phase boundaries, the periodicity along the AC direction can be satisfied, and thus a periodic sheet rather than nanoribbons is adopted as the model structure.

All the DFT calculations were performed by employing the Vienna *ab initio* simulation package (VASP)[46,47] using the projector-augmented wave method.[48] The exchange–correlation functional was described by generalized gradient approximation (GGA) parametrized by Perdew, Burke, and Ernzerhof.[49,50] For electronic structure calculations, we also performed additional benchmark calculations using other exchange–correlation functionals, *e.g.*, HSE06,[51] and confirmed that the results were not much affected by the usage of different functionals (for details see Section S2 in the ESI†). A kinetic cutoff energy of 550 eV was set for the plane-wave basis functions. All the structures were relaxed until the atomic forces were less than 0.01 eV $Å^{-1}$ and the

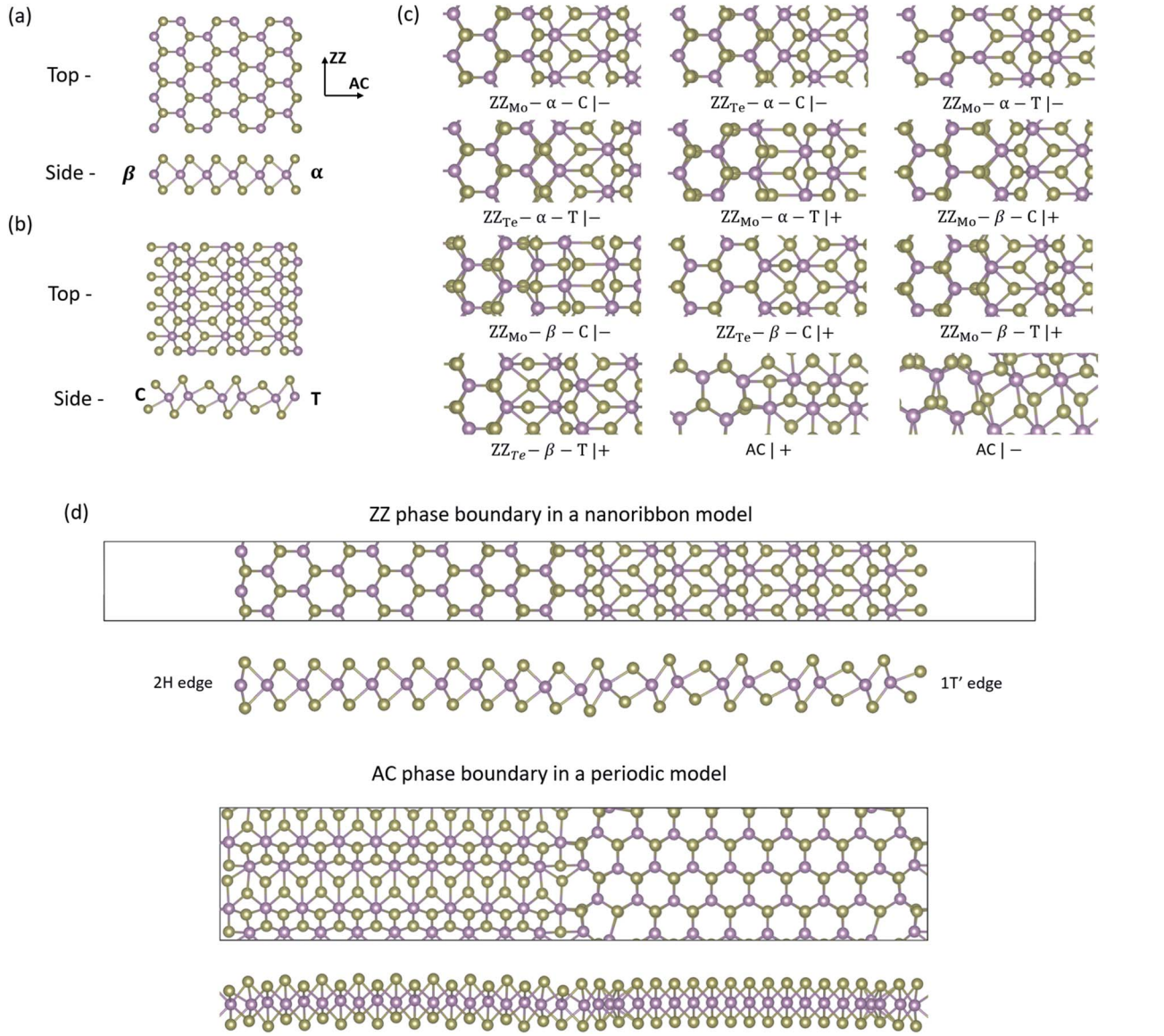

Fig. 1 The top and side views of pristine (a) 2H and (b) 1T′ $MoTe_2$, where Mo atoms are shown in purple and Te atoms are shown in brown, with the black arrows indicating the AC and ZZ directions of the $MoTe_2$ lattice. Two types of 2H edges (*i.e.*, α and β) and 1T′ edges (*i.e.*, C and T) are indicated in the side view. (c) The relaxed configurations of the twelve 2H/1T′ phase boundaries examined, named following the convention suggested by Zhao *et al.*[44] (d) The top and side views of a representative ZZ phase boundary, ZZ_{Mo}–α–C|− embedded in a nanoribbon model with 2H and 1T′ edges at each side, and an AC phase boundary AC|+ embedded in a periodic sheet model.

total energies were converged to 10^{-5} eV. Given that hydrogen adsorption and HER characteristics would be affected by hydrogen coverage, we considered different hydrogen coverages, ranging from 25% to 100%. Nonetheless, for simplicity and clarity of presentation, the results presented below mostly correspond to a hydrogen coverage of 50%. Additionally, in the calculations of hydrogen adsorption, the effect of van der Waals (vdW) interactions was included using the DFT-D3 method.[52,53]

Results and discussion

Formation energies of $MoTe_2$ phase boundaries

Before evaluating the hydrogen adsorption and HER at $MoTe_2$ phase boundaries, we first investigate the formation energies of the phase boundaries. For a ZZ phase boundary, its formation energy E_f can be determined from the total energy of the structure E_T as the following:[32]

$$E_T = N_{Mo}\mu_{Mo} + N_{Te}\mu_{Te} + L(\sigma_H + \sigma_{T'} + E_f) \quad (1)$$

where N_{Mo} and N_{Te} are the number of Mo and Te atoms at the phase boundary respectively, L is the phase boundary length, σ_H and $\sigma_{T'}$ are the formation energies of 2H and 1T′ edges per unit length, which can be obtained from separate calculations (for details see Section S3 in the ESI†), and μ_{Mo} and μ_{Te} are the chemical potentials of Mo and Te respectively. To maintain thermodynamic equilibrium, the allowable range of μ_{Te} and μ_{Mo} is constrained by the following condition:

$$\mu_{MoTe_2} = \mu_{Mo} + 2\mu_{Te} \quad (2)$$

where μ_{MoTe_2} represents the average weighted chemical potential of 2H and 1T′ phases. μ_{Te} varies depending on the chemical environment, assuming higher and lower values under Te-rich and Mo-rich conditions, respectively. The upper and lower limits of μ_{Te} can be regarded as being defined by the chemical potentials of alpha Te and body-centered cubic Mo respectively, thus ranging from −3.54 eV to −3.14 eV. The details of formation energy calculation can be found in the ESI.†

For AC phase boundaries, the periodic structures are constructed (*cf.* Fig. 1(d)), and the total energy of the structure can be written as:

$$E_T = N_{Mo}\mu_{Mo} + N_{Te}\mu_{Te} + 2E_fL \quad (3)$$

From eqn (1) and (3), the formation energy E_f can then be determined. The E_f values of various phase boundaries as functions of μ_{Te} are shown in Fig. 2. The lowest energy phase boundary is found to be the ZZ_{Mo}–α–C|− boundary under Mo-rich conditions (−3.54 eV < μ_{Te} < −3.27 eV), while it becomes the ZZ_{Mo}–β–T|+ boundary when the environment becomes Te-rich (−3.27 eV ≤ μ_{Te} < −3.14 eV). These results are in agreement with those of recent studies on the ZZ phase boundaries of $MoTe_2$.[32] Further analyses reveal that the formation energy of a phase boundary is strongly correlated with the local bond distortion. For instance, the ZZ_{Te}–β–C|+ boundary, the one with the highest formation energy, exhibits the most significant Mo–Te bond elongation/shrinkage at the boundary (for details see Section S4 in the ESI†). This large bond length variation induces significant mechanical stress/strain, leading to increase in the formation energy. In comparison, the bond distortion at low formation energy boundaries, *e.g.*, ZZ_{Mo}–β–C|− boundary, is much moderate (see Fig. S4†). It is also worth noting from Fig. 2 that the phase boundaries rich in Te (S = +) and deficient in Te (S = −) show opposite dependence on μ_{Te}, *i.e.*, E_f respectively increasing and decreasing monotonically as μ_{Te} increases. Such opposite dependence is directly related to the sign of the N_{Te} value, which is positive and negative for phase boundaries rich in Te (S = +) and deficient in Te (S = −) respectively.

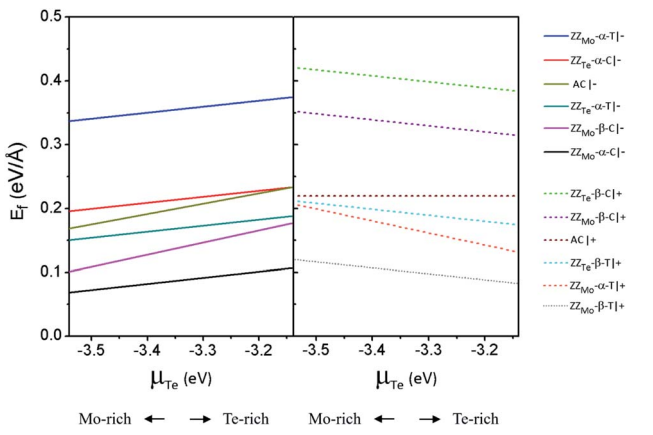

Fig. 2 Formation energies of the phase boundaries as functions of the chemical potential of Te, μ_{Te}.

With lower formation energy indicative of better stability and easier formation, consequently we only consider the two low-energy boundaries below, *i.e.*, ZZ_{Mo}–α–C|− and ZZ_{Mo}–β–T|+ for our investigation on HER activities. Further for the energy evaluation, we have also performed *ab initio* molecular dynamics (AIMD) simulations for ZZ_{Mo}–α–C|− and ZZ_{Mo}–β–T|+ boundaries to confirm their thermal stability at room temperature (for details please see Section S5 in the ESI†).

Hydrogen adsorption at $MoTe_2$ phase boundaries

To investigate the HER at the two phase boundaries ZZ_{Mo}–α–C|− and ZZ_{Mo}–β–T|+, we first identify the possible hydrogen adsorption sites at the boundary. These sites are illustrated in Fig. 3(a) and (c). As seen from the figure, we note that in the vicinity of the phase boundary hydrogen may adsorb at the hollow site (the triangle site surrounded by three adjacent Mo atoms in the middle of the three-layered structures, for details see Section S6 in the ESI†), or immediately above Mo or Te atoms. It should be noted that in addition to these sites mentioned above, we have also considered possible hydrogen adsorption at the bridge site (site between two Te atoms). However, our results show that the interaction between hydrogen and the bridge site is rather weak, making it an unstable adsorption site for hydrogen, as a result of which a hydrogen atom initially placed at the bridge site will move to its immediate neighboring Mo or Te site. Therefore, we only consider the stable adsorption sites below, namely Te, Mo, and hollow sites. For simplicity in describing these adsorption sites, we refer to the hollow site as HL, while the sites immediately above Mo or Te atoms as X_n where X = Mo or Te and n is an integer indicating the n^{th} site associated with the X atom below. In comparison to these sites at phase boundaries, their corresponding counterparts in pristine 2H and 1T′ lattices of $MoTe_2$ are also identified (illustrated in Fig. S7, see the ESI†) and examined as the respective reference sites.

One of the first steps of the HER is hydrogen adsorption (*i.e.*, the Volmer step) at the electrode surface. Generally, to achieve good catalytic performance, the binding between hydrogen and the electrode surface should be neither too strong nor too weak. Accordingly, it is desirable for hydrogen adsorption to have a Gibbs free energy ΔG_H close to the thermoneutral value near zero. The Gibbs free energy ΔG_H can be calculated as follows:[54]

$$\Delta G_H = \Delta E_H + \Delta E_{ZPE} - T\Delta S_H \quad (4)$$

where ΔE_H is the adsorption energy of the n^{th} H atom and is defined as:

$$\Delta E_H = E_{MoTe_2+nH} - E_{MoTe_2+(n-1)H} - \frac{1}{2}E_{H_2} \quad (5)$$

where E_{MoTe_2+nH} is the total energy of the $MoTe_2$ phase boundary with adsorbed hydrogen atoms, $E_{MoTe_2+(n-1)H}$ is the total energy of the $MoTe_2$ phase boundary without adding a hydrogen atom, and E_{H_2} is the energy of a gas phase hydrogen molecule. ΔE_{ZPE} is the difference in the zero-point energy of hydrogen in the adsorbed state and the gas phase. Our benchmark calculations have confirmed that vibrational frequencies do not differ

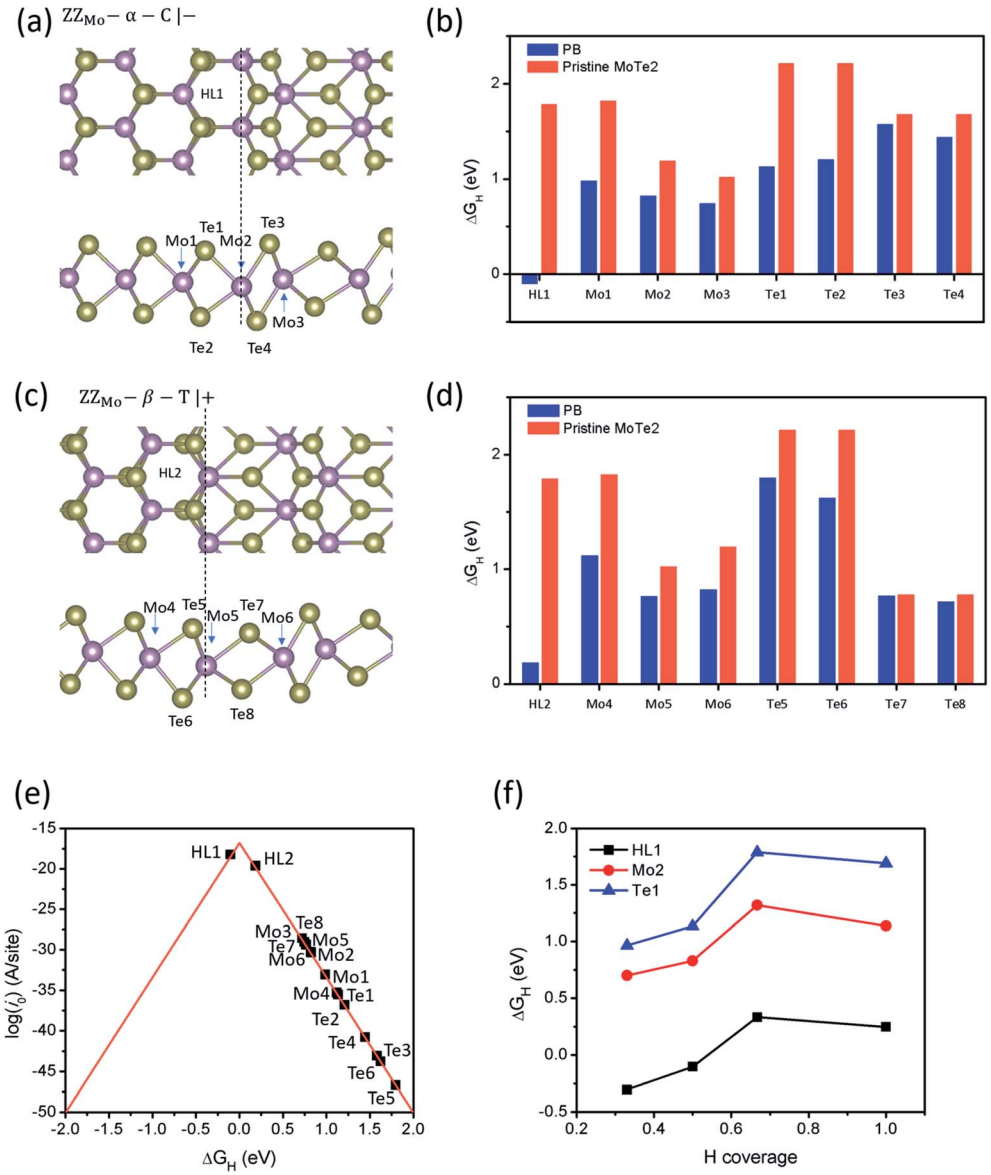

Fig. 3 (a) and (c) Adsorption sites of ZZ_{Mo}–α–C|− and ZZ_{Mo}–β–T|+ phase boundaries respectively. Adsorption sites are labeled by hollow (HL), Mo, and Te categories, respectively. (b) and (d) ΔG_H values of ZZ_{Mo}–α–C|− and ZZ_{Mo}–β–T|+ phase boundaries, compared with the respective adsorption energies on pristine $MoTe_2$ at the representative hydrogen coverage of 50%. For Mo2 or Mo5 sites, there exist two corresponding sites, in either the pristine 2H or 1T′ $MoTe_2$ lattice, and we only presented the pristine lattice site of lower ΔG_H here for comparison. (e) Volcano plot between the theoretical exchange current density i_0 and Gibbs free energy ΔG_H. (f) ΔG_H as a function of hydrogen coverage for three sites, HL1, Mo2 and Te1.

notably for different hydrogen coverages and structures, and that there is little variation in ΔE_{ZPE}. Consequently ΔE_{ZPE} is simply taken to be a constant value (*i.e.*, 0.02 eV). ΔS_H is the entropy term approximated as half of the entropy of the gas phase H_2 as $\Delta S_H \approx \frac{1}{2} S_{H_2}$.[55] T is the temperature, taken to be the room temperature ($T = 298$ K) in our study. Under ambient conditions, the term $T\Delta S_H$ approximately assumes a value of 0.2 eV and thus eqn (4) becomes:

$$\Delta G_H = \Delta E_H + 0.22 \text{ eV} \quad (6)$$

The Gibbs free energies of hydrogen adsorption at various sites in the boundary regions of ZZ_{Mo}–α–C|− and ZZ_{Mo}–β–T|+ respectively were examined. These values are presented in Fig. 3(b) and (d), in comparison with the corresponding energies at the respective counterpart sites on pristine 2H or 1T′ $MoTe_2$. As mentioned earlier in Section 2, the results correspond to a hydrogen coverage of 50%. It should be noted that the Mo atoms connecting the 2H and 1T′ phases of $MoTe_2$ at the boundary have two corresponding sites from pristine 2H and 1T′ $MoTe_2$ respectively, in which case only the site of lower ΔG_H is considered for comparison. It is apparent from Fig. 3 that the phase boundaries render ΔG_H lower and closer to zero

compared to pristine 2H or 1T′ $MoTe_2$, indicative of the improved HER activity at the phase boundary. Moreover, by examining the difference in the adsorption energy (between a site at the phase boundary and its reference site in the pristine 2H or 1T′ lattice), we note that the difference is more significant for sites on the 2H phase side. One salient observation from Fig. 3 is that hollow sites at phase boundaries exhibit near-zero ΔG_H values, in sharp contrast to their counterparts in the pristine $MoTe_2$. In particular, ΔG_H of the hollow site at ZZ_{Mo}–α–C|– shows a negative value close to zero ($\Delta G_H = -0.10$ eV), exhibiting strong adsorption of hydrogen, which is comparable to that of Pt ($\Delta G_H = -0.09$ eV).[14] These results suggest that hollow sites at phase boundaries may result in drastic boost to the HER activity. It is also important to recognize that the HER is a multistep electrochemical process. In this regard, we have also examined the subsequent steps beyond the Volmer step, and confirmed the Volmer step to be the determining step for the overall HER performance (for details see Section S8 in the ESI†).

Further calculations have also been performed to examine the generality of our results above. In particular, nearly identical hydrogen adsorption behaviors (*e.g.*, ΔG_H) at different sites were also found for few-layer $MoTe_2$ nanosheets (for details see Section S9 in the ESI†). Furthermore, we also confirmed that similar phase boundary induced HER enhancement exists in other TMDC systems, thus likely a generic phenomenon (for details see Section S10 in the ESI†).

To further evaluate the implications of the phase boundary for HER performance, a volcano curve is plotted as shown in Fig. 3(e). In the plot, the theoretical exchange current density i_0 is calculated based on the Gibbs free energy ΔG_H. The adsorption sites with a negative ΔG_H are located around the left leg of the volcano, and the i_0 at pH 0 can be calculated using the following expression:

$$i_0 = -ek_0 \frac{1}{1+\exp(-\Delta G_H/k_B T)} \quad (7)$$

where k_0 is the rate constant with a value of 200 s per site fitted to give a reasonable overall magnitude of the rate, and k_B is the Boltzmann constant. For the other case where adsorption sites are located around the right leg of the volcano (ΔG_H is positive), the i_0 is given by:

$$i_0 = -ek_0 \frac{1}{1+\exp(-\Delta G_H/k_B T)} \exp(-\Delta G_H/k_B T) \quad (8)$$

Adsorption sites with ΔG_H close to zero are located at the peak of the volcano curve, indicating the highest exchange current density and the optimal HER performance. We find that two hollow sites are located very close to the peak of the volcano curve with a very high exchange current density, suggesting that they are the potential sites to offer the best performance at the boundaries. Meanwhile, the influence of hydrogen coverage on ΔG_H is illustrated in Fig. 3(f). As seen in the figure, with the sites HL1, Mo2 and Te1 as representatives, we see that ΔG_H as a function of hydrogen coverage, exhibits a similar trend for different adsorption sites with the hollow sites always remaining to be the ones with the smallest $|\Delta G_H|$ values. As the hydrogen coverage increases, ΔG_H first increases until a coverage ~70%, followed by a slight decrease with further increase in the coverage. In particular, for the HL1 site shown in Fig. 3(f), one can see that the free energy close to zero occurs around 50–60% hydrogen coverage, indicative of an optimal coverage for the HER. Increasing hydrogen coverage beyond this range would increase ΔG_H (>0) for all the sites, thus expected to lower the HER activity. On the other hand, decreasing hydrogen coverage below this range, though negatively impacting the hollow sites, renders the ΔG_H values of other sites closer to zero. Therefore, Fig. 3(f) also suggests more effective HER performance with hydrogen adsorption below 60% coverage.

Overall, our calculations above confirmed that the phase boundaries in $MoTe_2$ can provide active sites with significantly better hydrogen adsorption characteristics, thus potentially contributing to boosting of the overall HER performance of $MoTe_2$.

Relation between hydrogen adsorption and electronic properties

The key characteristics of a catalyst are fundamentally determined by their electronic structures. In this regard, we have performed comprehensive analysis of the electronic structures of phase boundary containing $MoTe_2$ systems to further understand the interaction between hydrogen and the various adsorption sites at the phase boundary. Generally, not every electronic state in the band contributes equally to the bonding between hydrogen and the adsorption site. Huang *et al.* revealed that the closer an electronic state is to the Fermi level (E_F), the greater is its contribution to the bonding.[56] By examining the density of states (DOS), we analyzed the states associated with different adsorption sites, with reference to the Fermi level. Some sample analysis is shown in Fig. 4(a), where the two Te adsorption sites, Te1 and Te5 (*cf.* Fig. 3), are compared (DOS of other Te sites is also examined, see Fig. S11 in the ESI†). As noted from the figure, the Te1 site has more occupied states near the E_F compared to Te5, and is thus expected to have stronger hydrogen adsorption. This prediction based on the electronic analysis agrees well with the ΔG_H results, *i.e.*, $\Delta G_{H\text{–}Te1} = 1.13$ eV < $\Delta G_{H\text{–}Te5} = 1.80$ eV (*cf.* Fig. 3 above).

To further quantitatively understand the relation between ΔG_H and the electronic structure, we note that, according to the Fermi-abundance (D_F) model,[15,56,57] the band structures of adsorption sites can be described by the following equation:

$$D_F = \frac{\int_{-\infty}^{E_F} ED(E) f'_T(E-E_F)\mathrm{d}E}{\int_{-\infty}^{E_F} D(E) f'_T(E-E_F)\mathrm{d}E} \quad (9)$$

where $D(E)$ is the density of states, and $-f'_T(E-E_F)$ is the derivative of the Fermi–Dirac distribution function $f_T(E-E_F) = \{\exp[(E-E_F)/k_BT]+1\}^{-1}$, used as an effective weight factor $w(E)$ to evaluate the contribution of every electronic state to the surface reaction. The spreading of the $w(E)$ is sensitive to the

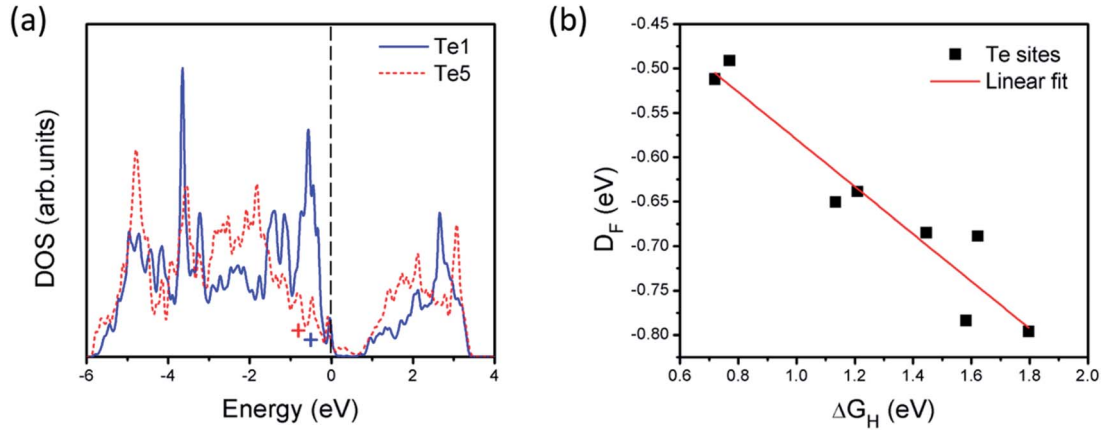

Fig. 4 (a) DOS of two representative Te atoms for H adsorption sites. The symbol "+" labels the position of the Fermi-abundance center (D_F). (b) Relationship between D_F values and ΔG_H for Te atoms.

magnitude of k_BT, where k_B is Boltzmann's constant and T is not the actual temperature but a parametric temperature,[15,56] and thus k_BT serves as an adjustable parameter to tune the weight factor. As suggested by previous studies,[15,56] when k_BT assumes a value of 0.4 eV, optimal correlation can be achieved between D_F and the surface bonding and reactivity, and in particular, ΔG_H of hydrogen adsorption would exhibit a linear trend with the D_F of the catalyst.

Guided by the above model, we then analyzed the relationship between the HER activities of various sites at phase boundaries and their corresponding electronic structures. We started by examining the group of Te sites at ZZ_{Mo}–α–C|− and ZZ_{Mo}–β–T|+ boundaries. Fig. 4(b) shows the D_F values of various Te sites *versus* the corresponding ΔG_H values. An apparent linear relation between D_F and ΔG_H can be observed, with a larger D_F indicating stronger H–Te bonding. This suggests that D_F serves as a good metric to quantify the HER activity of Te sites at $MoTe_2$ phase boundaries. The Fermi-abundance model is also expected to apply to a broad class of other adsorption sites in both phase boundaries and pristine lattices, where hydrogen predominately interacts with a single host atom at the adsorption site (see below for further discussion).[15,57]

However, despite the success of the Fermi-abundance model in describing the Te sites, it fails to yield good representation of the HER activity at other sites, *i.e.*, the Mo and hollow sites, at $MoTe_2$ phase boundaries, as demonstrated in Fig. S12 (for details see Section S12 in the ESI†). This indicates a clear limitation of the Fermi-abundance model. To understand this limitation, we took a closer look at these Mo and hollow sites at phase boundaries. For insights into how hydrogen interacts with atoms at different sites, we examined the charge distribution contour associated with hydrogen adsorption, based on the spatial charge density difference $\Delta\rho(r)$:

$$\Delta\rho(r) = \rho_{PB-H}(r) - \rho_{PB}(r) - \rho_H(r) \quad (10)$$

where $\rho_{PB-H}(r)$ and $\rho_{PB}(r)$ are the space charge densities of the phase boundaries with and without hydrogen adsorption, at location r. $\rho_H(r)$ is the electron charge density of a hydrogen atom at the same position in a reference pristine supercell. The obtained charge distribution contours of phase boundaries with H adsorbed on Te1, Mo1 and HL1 sites are shown in Fig. 5(a)–(c) as representatives of the three types of adsorption sites (see Fig. S13 and S14 in the ESI† for the charge distributions of other adsorption configurations). The yellow and cyan colors in the contour indicate the gain and loss of charges respectively, indicative of the overlap of various orbitals from different atoms. For adsorption at the Te1 site, we see from Fig. 5(a) that hydrogen mostly interacts with the Te atom alone, showing a clear charge gain of hydrogen from Te, whereas the interactions between hydrogen and other atoms are negligible. Now upon examining the Mo1 site, we see from Fig. 5(b) that hydrogen not only interacts with the Mo atom, but also with the surrounding Te atoms. Apart from a charge transfer from Mo and H atoms, there is an apparent loss of charges from neighboring Te atoms to H atoms. The difference in the local atomic interactions at Te1 and Mo1 sites is also well reflected in the DOS plots. As seen from Fig. 5(d), one can see that for the Te1 site, only the states of the Te atom diminish significantly upon hydrogen adsorption. The 5s and 5p states of the Te atom hybridize with the 1s state of hydrogen to result in the energy splitting and the formation of new bonding states. In comparison, for the Mo1 site, decrease in the states of both Mo and Te atoms near the Fermi level can be observed. The hybridization of the 1s state of hydrogen with the 5s and 5p bonding states of the Te atom and the 4d bonding states of the Mo atom results in the formation of new bonding states. Therefore, with multiple orbitals from different atoms taking part in the interaction between the H atom and the catalyst, the Fermi-abundance model is no longer suitable to describe the HER activity at Mo sites. Nonetheless, despite quantitative assessment of the activation at Mo sites being not possible, qualitative evaluation based on the DOS plots is possible. As shown in Fig. S15 (see the ESI†), the Mo sites at phase boundaries have more occupied states near the E_F compared to their counterparts in the pristine lattice, and are thus expected to have stronger hydrogen adsorption.

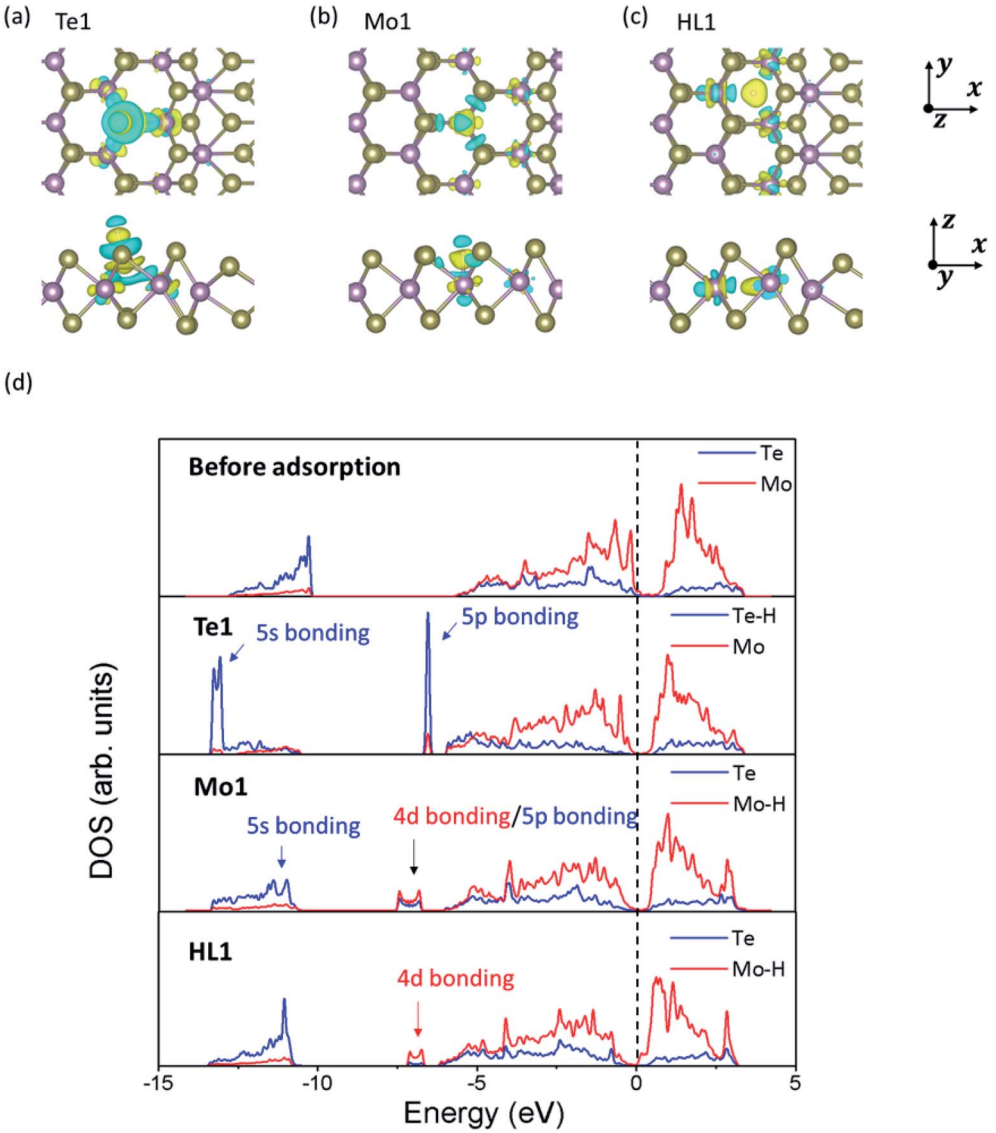

Fig. 5 Charge distribution contour plots for hydrogen adsorption sites: (a) Te1, (b) Mo1 and (c) HL1 sites at the $MoTe_2$ phase boundary. The yellow and cyan surfaces correspond to the gain and loss of charge respectively, with an isosurface of 0.003 e $Å^{-3}$. (d) DOS plots for Te and Mo atoms respectively (top panel) before hydrogen adsorption, (second panel) after hydrogen adsorption on the Te1 site, (third panel) after hydrogen adsorption at the Mo1 site, and (bottom panel) after hydrogen adsorption at the HL1 site.

The HL site resembles the Mo1 site in the fact that hydrogen adsorption also involves multiple atoms. As shown in Fig. 5(c), hydrogen adsorbed at the HL site does not sit on top of an individual atom but in the close vicinity of three adjacent Mo atoms along the x and y plane, showing a clear charge gain of hydrogen from these Mo atoms. Similar to what is described above for the Mo1 site, hydrogen adsorption at the HL site may also be understood by examining the Mo atoms hydrogen interacts with. Fig. 5(d) shows the DOS plots of Mo and Te atoms after hydrogen adsorption at the HL1 site. We can see that the 4d states of the Mo atom hybridize with the 1s state of hydrogen, resulting in the formation of new bonding states, while the DOS of the Te atom remains nearly unchanged with no new bonding states formed post adsorption. Thus, the interaction between multiple Mo atoms and the H atom occurs and causes the failure of the Fermi-abundance model to describe the HER activity at the HL sites. However, the activations at HL sites can still be evaluated based on the DOS plots of the Mo atoms (see Fig. S15 in the ESI†).

The above analysis of the electronic structures provides us with critical insights for assessing hydrogen adsorption. However, why only HL sites exhibit optimal adsorption performance remains a puzzle (with near zero ΔG_H, *cf.* Fig. 3). Fig. 6 shows the projected density of states (pDOS) of the 4d orbitals of the Mo atom (*i.e.*, the Mo1 atom) shared by the Mo1 and HL1 sites, for hydrogen adsorption at the Mo1 and HL1 sites respectively. One can see that the 4d states yield a high peak near the Fermi level (prior to hydrogen adsorption), indicating its great contribution to the bonding. Specifically, these orbitals are d_{xy} and $d_{x^2-y^2}$ orbitals. In order to form a strong bonding

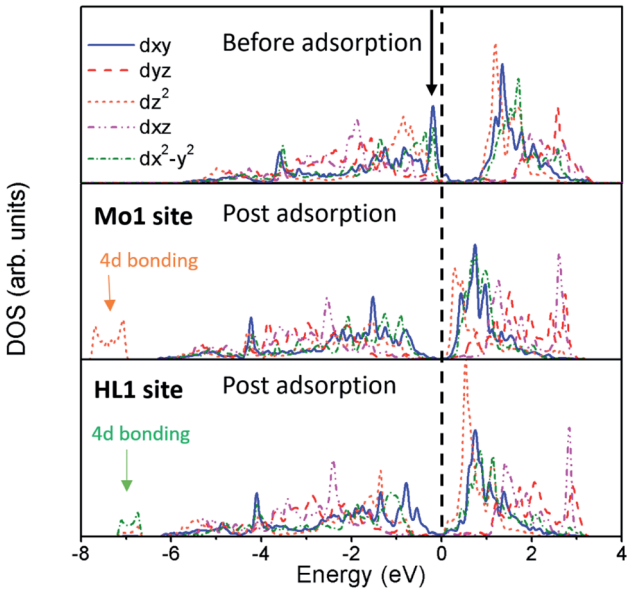

Fig. 6 Projected DOS (pDOS) plots for the d orbitals of the Mo1 atom along the $MoTe_2$ phase boundary, (top panel) before adsorption, after adsorption on the Mo1 site, and after adsorption on the HL1 site. The black arrow indicates the reinforcing states of d_{xy} and $d_{x^2-y^2}$ orbitals near the Fermi level.

upon hydrogen adsorption, it is preferable to have an overlap between the 1s orbital of hydrogen and the d_{xy} or $d_{x^2-y^2}$ orbital of the Mo atom, while overlap between 1s of hydrogen and other d orbitals (*e.g.* d_{z^2}) of Mo is less desirable and would render the Mo–H bond weaker.

Upon hydrogen adsorption, we see from Fig. 5(b) that, for adsorption at the Mo1 site, the distribution of electronic charge shows the orbital character of d_{z^2}, indicating the interaction between Mo d_{z^2} and hydrogen 1s. Also, from the pDOS plot in Fig. 6, we can see that the new 4d bonding state post hydrogen adsorption at the Mo1 site mainly originates from the d_{z^2} states. In contrast, for hydrogen adsorption at the HL1 site, it mainly interacts with the d orbitals of three adjacent Mo atoms parallel with the *xy* plane, *i.e.* d_{xy} or $d_{x^2-y^2}$ orbitals (*cf.* Fig. 5(c)), with the distribution of electronic charge of Mo atoms showing apparent $d_{x^2-y^2}$ and d_{xy} characteristics. Accordingly, as seen from the pDOS plot in Fig. 6, the $d_{x^2-y^2}$ orbital contributes the most to the formation of 4d bonding states for the case of the HL1 site (for another Mo atom neighboring the HL1 site, the d_{xy} orbital contributes the most to the formation of 4d bonding states, see Fig. S16 in the ESI†). This bonding corresponds to the strong hydrogen adsorption, hence resulting in optimal hydrogen adsorption at HL sites.

Conclusion

In summary, comprehensive first-principles calculations have been performed to investigate the HER activities at the phase boundaries in TMDCs, using $MoTe_2$ as a representative. Possible 2H/1T′ phase boundaries have been constructed, with their structural stability and formation energies examined to identify stable configurations. Three categories of sites, namely Te, Mo and hollow sites, at energetically stable phase boundaries were identified as potential catalytic centers for the HER. All these sites were demonstrated to activate hydrogen adsorption by reducing the magnitude of the Gibbs free energy ΔG_H, promising for enhancement of the HER activity. In particular, the hollow sites were found to exhibit ΔG_H near the thermoneutral value, comparable to that of Pt at moderate hydrogen coverages. The mechanisms underlying such activation at phase boundaries were then revealed, and found to be attributed to the unique local hydrogen adsorption geometries and electronic structures at the phase boundaries. Specifically, for the Te sites where hydrogen interacts almost solely with the host atom (*i.e.*, Te), the catalytic activity is well understood and predicted using the Fermi-abundance model. The Fermi-abundance model and similar interpretation are also expected to apply to a broad class of other adsorption sites in both phase boundaries and pristine lattices, where hydrogen predominately interacts with a single host atom at the adsorption site. However, the Fermi-abundance model breaks down for the Mo and hollow sites where hydrogen adsorption assumes a more complex geometry and involves multiple atoms, though qualitative assessment can still be made by analyzing the local charge distribution and density of states. In addition, we elucidated that the optimal hydrogen adsorption performance at the hollow sites originates from the fact that the phase boundary modifies the d_{xy} and $d_{x^2-y^2}$ orbitals of Mo atoms, thus giving rise to much stronger binding with hydrogen.

Our study demonstrates a viable pathway to activate the basal plane of 2D TMDCs for the HER through phase boundary engineering and clarifies the important mechanistic aspects underlying hydrogen activation at phase boundaries, providing valuable theoretical insights into designing a new class of high-performance HER electrocatalysts based on 2D TMDCs.

Conflicts of interest

There are no conflicts to declare.

Acknowledgements

This research was supported by the Natural Sciences and Engineering Research Council of Canada (NSERC) Discovery Grant (grant #: NSERC RGPIN-2017-05187), and the McGill Engineering Doctoral Award (MEDA). The authors would also like to acknowledge the Compute Canada and Calcul Québec for providing computing resources.

References

1 J. A. Turner, *Science*, 2004, **305**, 972–974.
2 S. Trasatti, *J. Electroanal. Chem. Interfacial Electrochem.*, 1972, **39**, 163–184.
3 N. Cheng, S. Stambula, D. Wang, M. N. Banis, J. Liu, A. Riese, B. Xiao, R. Li, T. K. Sham, L. M. Liu, G. A. Botton and X. Sun, *Nat. Commun.*, 2016, **7**, 13638.

4 Y. Jiao, Y. Zheng, M. Jaroniec and S. Z. Qiao, *Chem. Soc. Rev.*, 2015, **44**, 2060–2086.
5 A. B. Laursen, S. Kegnæs, S. Dahl and I. Chorkendorff, *Energy Environ. Sci.*, 2012, **5**, 5577–5591.
6 T. F. Jaramillo, K. P. Jørgensen, J. Bonde, J. H. Nielsen, S. Horch and I. Chorkendorff, *Science*, 2007, **317**, 100–102.
7 B. Hinnemann, P. G. Moses, J. Bonde, K. P. Jørgensen, J. H. Nielsen, S. Horch, I. Chorkendorff and J. K. Nørskov, *J. Am. Chem. Soc.*, 2005, **127**, 5308–5309.
8 Y. R. An, X. L. Fan, Z. F. Luo and W. M. Lau, *Nano Lett.*, 2017, **17**, 368–376.
9 B. Hinnemann, P. G. Moses, J. Bonde, K. P. Jørgensen, J. H. Nielsen, S. Horch, I. Chorkendorff and J. K. Nørskov, *J. Am. Chem. Soc.*, 2005, **127**, 5308–5309.
10 Y. Chen, K. Yang, B. Jiang, J. Li, M. Zeng and L. Fu, *J. Mater. Chem. A*, 2017, **5**, 8187–8208.
11 C. R. Zhu, D. Gao, J. Ding, D. Chao and J. Wang, *Chem. Soc. Rev.*, 2018, **47**, 4332–4356.
12 M. Liu, M. S. Hybertsen and Q. Wu, *Angew. Chem., Int. Ed.*, 2020, **59**, 14835–14841.
13 C. Wang, H. Lu, K. Tang, Z. Mao, Q. Li, X. Wang and C. Yan, *Electrochim. Acta*, 2020, **336**, 135740.
14 Y. Ouyang, C. Ling, Q. Chen, Z. Wang, L. Shi and J. Wang, *Chem. Mater.*, 2016, **28**, 4390–4396.
15 H. Shu, D. Zhou, F. Li, D. Cao and X. Chen, *ACS Appl. Mater. Interfaces*, 2017, **9**, 42688–42698.
16 C. Tsai, K. Chan, F. Abild-Pedersen and J. K. Norskov, *Phys. Chem. Chem. Phys.*, 2014, **16**, 13156–13164.
17 J. Zhu, Z. C. Wang, H. Dai, Q. Wang, R. Yang, H. Yu, M. Liao, J. Zhang, W. Chen, Z. Wei, N. Li, L. Du, D. Shi, W. Wang, L. Zhang, Y. Jiang and G. Zhang, *Nat. Commun.*, 2019, **10**, 1348.
18 D. Voiry, M. Salehi, R. Silva, T. Fujita, M. Chen, T. Asefa, V. B. Shenoy, G. Eda and M. Chhowalla, *Nano Lett.*, 2013, **13**, 6222–6227.
19 M. A. Lukowski, A. S. Daniel, F. Meng, A. Forticaux, L. Li and S. Jin, *J. Am. Chem. Soc.*, 2013, **135**, 10274–10277.
20 Q. Tang and D. E. Jiang, *ACS Catal.*, 2016, **6**, 4953–4961.
21 M. Calandra, *Phys. Rev. B: Condens. Matter Mater. Phys.*, 2013, **88**, 245428.
22 D. Wang, X. Zhang, S. Bao, Z. Zhang, H. Fei and Z. Wu, *J. Mater. Chem. A*, 2017, **5**, 2681–2688.
23 S. Kim, J. H. Kim, D. Kim, G. Hwang, J. Baik, H. Yang and S. Cho, *2D Mater.*, 2017, **4**, 024004.
24 Y. Yu, G.-H. Nam, Q. He, X.-J. Wu, K. Zhang, Z. Yang, J. Chen, Q. Ma, M. Zhao and Z. Liu, *Nat. Chem.*, 2018, **10**, 638–643.
25 L. Li, Z. Qin, L. Ries, S. Hong, T. Michel, J. Yang, C. Salameh, M. Bechelany, P. Miele, D. Kaplan, M. Chhowalla and D. Voiry, *ACS Nano*, 2019, **13**, 6824–6834.
26 P. Valerius, S. Kretschmer, B. V. Senkovskiy, S. Wu, J. Hall, A. Herman, N. Ehlen, M. Ghorbani-Asl, A. Grueneis and A. V. Krasheninnikov, *2D Mater.*, 2020, **7**, 025005.
27 R. Zhao, Y. Wang, D. Deng, X. Luo, W. J. Lu, Y.-P. Sun, Z.-K. Liu, L.-Q. Chen and J. Robinson, *Nano Lett.*, 2017, **17**, 3471–3477.
28 S.-W. Wang, H. Medina, K.-B. Hong, C.-C. Wu, Y. Qu, A. Manikandan, T.-Y. Su, P.-T. Lee, Z.-Q. Huang, Z. Wang, F.-C. Chuang, H.-C. Kuo and Y.-L. Chueh, *ACS Nano*, 2017, **11**, 8768–8776.
29 S. Song, D. H. Keum, S. Cho, D. Perello, Y. Kim and Y. H. Lee, *Nano Lett.*, 2016, **16**, 188–193.
30 J. H. Sung, H. Heo, S. Si, Y. H. Kim, H. R. Noh, K. Song, J. Kim, C. S. Lee, S. Y. Seo, D. H. Kim, H. K. Kim, H. W. Yeom, T. H. Kim, S. Y. Choi, J. S. Kim and M. H. Jo, *Nat. Nanotechnol.*, 2017, **12**, 1064–1070.
31 K. A. Duerloo and E. J. Reed, *ACS Nano*, 2016, **10**, 289–297.
32 A. Li, J. Pan, X. Dai and F. Ouyang, *J. Appl. Phys.*, 2019, **125**, 075104.
33 L. Zhou, K. Xu, A. Zubair, X. Zhang, F. Ouyang, T. Palacios, M. S. Dresselhaus, Y. Li and J. Kong, *Adv. Funct. Mater.*, 2017, **27**, 1603491.
34 X. Ji, K. Wang, Y. Zhang, H. Sun, Y. Zhang, T. Ma, Z. Ma, P. Hu and Y. Qiu, *Sustainable Energy Fuels*, 2020, **4**, 407–416.
35 X. Ji, Y. Zhang, Z. Ma and Y. Qiu, *ChemSusChem*, 2020, DOI: 10.1002/cssc.202001185.
36 Z. Zhuang, Y. Li, Z. Li, F. Lv, Z. Lang, K. Zhao, L. Zhou, L. Moskaleva, S. Guo and L. Mai, *Angew. Chem.*, 2018, **130**, 505–509.
37 W. Luo, M. Zhu, G. Peng, X. Zheng, F. Miao, S. Bai, X.-A. Zhang and S. Qin, *Adv. Funct. Mater.*, 2018, **28**, 1704539.
38 Y. Q. Bie, G. Grosso, M. Heuck, M. M. Furchi, Y. Cao, J. Zheng, D. Bunandar, E. Navarro-Moratalla, L. Zhou, D. K. Efetov, T. Taniguchi, K. Watanabe, J. Kong, D. Englund and P. Jarillo-Herrero, *Nat. Nanotechnol.*, 2017, **12**, 1124–1129.
39 Y. Zhou, J. L. Silva, J. M. Woods, J. V. Pondick, Q. Feng, Z. Liang, W. Liu, L. Lin, B. Deng, B. Brena, F. Xia, H. Peng, Z. Liu, H. Wang, C. M. Araujo and J. J. Cha, *Adv. Mater.*, 2018, **30**, e1706076.
40 D. Qi, Q. Wang, C. Han, J. Jiang, Y. Zheng, W. Chen, W. Zhang and A. T. S. Wee, *2D Mater.*, 2017, **4**, 045016.
41 D. H. Keum, S. Cho, J. H. Kim, D.-H. Choe, H.-J. Sung, M. Kan, H. Kang, J.-Y. Hwang, S. W. Kim, H. Yang, K. J. Chang and Y. H. Lee, *Nat. Phys.*, 2015, **11**, 482.
42 Y. Yin, J. Han, Y. Zhang, X. Zhang, P. Xu, Q. Yuan, L. Samad, X. Wang, Y. Wang, Z. Zhang, P. Zhang, X. Cao, B. Song and S. Jin, *J. Am. Chem. Soc.*, 2016, **138**, 7965–7972.
43 N. Zhao, L. Wang, Z. Zhang and Y. Li, *ACS Appl. Mater. Interfaces*, 2019, **11**, 42014–42020.
44 W. Zhao and F. Ding, *Nanoscale*, 2017, **9**, 2301–2309.
45 S. Zhou, J. Han, J. Sun and D. J. Srolovitz, *2D Mater.*, 2017, **4**, 025080.
46 G. Kresse and D. Joubert, *Phys. Rev. B: Condens. Matter Mater. Phys.*, 1999, **59**, 1758–1775.
47 G. Kresse and J. Furthmüller, *Phys. Rev. B: Condens. Matter Mater. Phys.*, 1996, **54**, 11169–11186.
48 P. E. Blöchl, *Phys. Rev. B: Condens. Matter Mater. Phys.*, 1994, **50**, 17953–17979.
49 J. P. Perdew, K. Burke and M. Ernzerhof, *Phys. Rev. Lett.*, 1996, **77**, 3865–3868.
50 J. P. Perdew, J. A. Chevary, S. H. Vosko, K. A. Jackson, M. R. Pederson, D. J. Singh and C. Fiolhais, *Phys. Rev. B: Condens. Matter Mater. Phys.*, 1992, **46**, 6671–6687.

51 J. Heyd, G. E. Scuseria and M. Ernzerhof, *J. Chem. Phys.*, 2003, **118**, 8207.
52 S. Grimme, J. Antony, S. Ehrlich and H. Krieg, *J. Chem. Phys.*, 2010, **132**, 154104.
53 S. Grimme, S. Ehrlich and L. Goerigk, *J. Comput. Chem.*, 2011, **32**, 1456–1465.
54 J. K. Nørskov, T. Bligaard, A. Logadottir, J. R. Kitchin, J. G. Chen, S. Pandelov and U. Stimming, *J. Electrochem. Soc.*, 2005, **152**, J23–J26.
55 C. Tsai, F. Abild-Pedersen and J. K. Nørskov, *Nano Lett.*, 2014, **14**, 1381–1387.
56 B. Huang, L. Xiao, J. Lu and L. Zhuang, *Angew. Chem., Int. Ed.*, 2016, **55**, 6239–6243.
57 Y. Zhang, X. Chen, Y. Huang, C. Zhang, F. Li and H. Shu, *J. Phys. Chem. C*, 2017, **121**, 1530–1536.